The Use of Magnetic Resonance Images in the Simulation of Diffusion in Porous Catalyst Support Pellets

Sean P. Rigby[1] and Lynn F. Gladden

Department of Chemical Engineering, University of Cambridge, Pembroke Street, Cambridge, CB2 3RA, United Kingdom

Previous work on the simulation of diffusion in porous materials and, in particular, catalyst support pellets has, in general, made use of abstract mathematical models to represent the structure of those materials. In this work a magnetic resonance image of the spatial distribution of voidage within a thin slice through a porous catalyst support pellet is used as the basis for a potentially more realistic representation of the porous structure. Simulations of diffusion are performed using a simulation lattice derived from the image and the resulting predictions of tortuosity are compared with experimentally determined values obtained using PGSE NMR and magnetic resonance imaging techniques. This approach is applied to the study of five different types of catalyst support pellet. © 1998 Academic Press

INTRODUCTION

When modelling diffusion within porous materials the general procedure usually involves developing a mathematical representation for the internal structure of a porous material and performing the simulations of diffusion within that model structure. The model structure might be a network of cylindrical pores (1–3), an agglomeration of spheres or rods (4–7) or a fractal representation (8, 9). Previous magnetic resonance imaging studies have suggested that diffusion within porous catalyst support pellets may be influenced by heterogeneities in the spatial distribution of voidage and pore size over macroscopic length scales (0.01–1.0 mm) (10, 11) and, further, that a porous catalyst produced by a given manufacturing process will be characterised by a particular clustering of regions of similar surface-to-volume ratio of the internal surface (12). The latter conclusion was drawn from the observation that the spin-lattice relaxation time images recorded for each pellet from a given batch were characterised by a constant fractal dimension. In earlier work we have investigated the possibility that numerical models based on lattices of

fractal character might therefore reflect at some level this variation in pore structure and, hence, be able to predict more accurately the diffusion phenomena occurring within the porous medium (13); this remains a subject of ongoing study.

In this paper an alternative approach is considered. One of the advantages of magnetic resonance imaging (MRI) techniques over other imaging methods is that the MRI measurement can be made sensitive to various physical and chemical parameters such as pore size, voidage, diffusion coefficient, and chemical species (10, 14). In this work, the spatial distribution of heterogeneity in voidage within a real pellet is imaged and from this image the lattice used for the simulations of diffusion is derived. The results of diffusion simulations are presented for five different types of porous catalyst pellet and the results compared with experimentally determined values of the tortuosity characterising the pore structure of these materials.

EXPERIMENTAL

The details of the pellets studied are given in Table 1. The procedure for obtaining spin density images of catalyst pellet samples has been reported in earlier work (10, 11) and therefore only relevant experimental parameters are presented here. Water is imbibed within the pore structure of the catalyst pellet and it is the ^{1}H signal from the water molecules which is detected in the NMR experiments discussed here. ^{1}H imaging experiments were performed using a Bruker DMX 200 NMR spectrometer with a static field strength of 4.7 T yielding a proton resonance frequency of 199.859 MHz. Shielded gradient coils were used and an airflow was maintained through these to prevent overheating arising from rapid switching of gradients. Imaging probe inserts of diameters 5 and 10 mm were used. For each insert, the response of the imaging coil as a function of position was determined for a water phantom and was found to be uniform over the volume occupied by the catalyst pellet samples. Each pellet was positioned in the probe so that the centre of the pellet coincided with the centre of the

[1] Present address: ICI Katalco, P.O. Box 1, Billingham, Cleveland, TS23 1LB, United Kingdom. E-mail: sean_p_rigby@ici.com.

TABLE 1

Results of the Characterisation, Using Mercury Porosimetry, of the Pellets Studied in This Work

Batch	Material	Surface area $(m^2\,g^{-1})$	Pore volume $(cm^3\,g^{-1})$	Voidage	Form
E1	Al_2O_3	120 ± 10	0.33 ± 0.03	0.49 ± 0.03	Tablet
E2	Al_2O_3	250 ± 20	0.67 ± 0.05	0.65 ± 0.03	Extrudate
E3	Al_2O_3	134 ± 12	0.44 ± 0.04	0.59 ± 0.03	Tablet
G1	SiO_2	440 ± 36	0.95 ± 0.05	0.66 ± 0.03	Gel sphere
G2	SiO_2	127 ± 10	0.94 ± 0.05	0.69 ± 0.03	Gel sphere

selected image slice. Images were acquired using a spin-echo pulse sequence employing 90° selective and 180° non-selective pulses, the imaging sequence was preconditioned using a saturation recovery pulse sequence and an echo time of 2.6 ms was used. The pulse lengths were typically 500 μs for the selective 90° pulse and 6.9 μs for the non-selective 180° pulse. The recycle time was always at least $5T_1$ and typically 1.5–3 s, depending on the sample, where T_1 is the average spin-lattice relaxation time of the water imbibed within the sample. The images obtained were of dimension 128×128 pixels acquired using read, phase, and slice gradient strengths of 33.09, 24.68, and 5.52 G cm^{-1}, respectively, thereby yielding an in-plane resolution of 40 μm. Slice selection was obtained using Gaussian rf pulses truncated at 5% of maximum intensity. Gradients in the z-direction were chosen to give slice thicknesses not greater than 30% of the sample diameter or length and in the range 0.3–1 mm. The T_1-contrast was obtained by varying the delay time between the nonselective 90° pulse of the saturation recovery preconditioning and the selective 90° pulse of the imaging pulse sequence. For each sample, eight images were acquired with the delay times, VD in Eq. [1] below, distributed over the range $0.1T_1 < VD < 5T_1$. It was ensured that the lower limit in the range of delay times exceeded three times the value of the spin–spin relaxation time, T_2, for the sample under study. The eight T_1-weighted images were then analysed to yield a spin density (ρ) image and a T_1-image by fitting the signal intensity, I, from the same pixel, i, in each of the eight images to the expression describing the relative contributions of T_1 and ρ to that signal intensity, where

$$I(i, VD) = \rho(i)[1 - \exp(-VD/T_1(i))], \qquad [1]$$

thus obtaining a value of spin density, $\rho(i)$, and $T_1(i)$ for the pixel i. By repeating the procedure for each pixel in the array, images of spin-density (corresponding to water concentration and, hence, a measure of voidage) and spin-lattice relaxation time within the sample were produced.

NUMERICAL MODELLING

Construction of the Simulation Lattice

The pixel intensities in the spin density image are on an arbitrary scale but are directly proportional to the voidage in that pixel. In order to render the image into a form in which the simulations of diffusion can be performed, the images were gated such that image pixels associated with an intensity below a certain value were assigned to be solid matrix and those with an intensity above this threshold value were assigned to be void space. The gating level was chosen so that the resulting two-dimensional lattice (shown in Fig. 1) had the same voidage as the real pellet. The largest possible square array of pixels was then cut from the image and divided up into an 8×8 grid, each square on the grid comprising a square subarray of the image pixels.

Simulation of Diffusion

Simulations of diffusion using two approaches previously described by Elias-Kohav *et al.* (8) were performed on the lattices derived from the magnetic resonance images. The two algorithms used are the whole object averaging and diffusion flux methods, the principles of which are outlined below.

Whole Object Averaging

In this approach the local tortuosity is approximated by the number of sideways diversions that a molecule needs to proceed in the void space. If M is the locally averaged number of blocked pixels adjacent to an empty site, then the probability of a one-pixel diversion is $M/4$ for the case of a 2D square lattice. After such a move there is a similar probability of a further diversion and, when M does not vary with every diversion, the local tortuosity after n steps is

$$\tau = 1 + \frac{M}{4} + \left(\frac{M}{4}\right)^2 + \cdots + \left(\frac{M}{4}\right)^n \rightarrow \frac{1}{1 - (M/4)}, \quad [2]$$

where the limit holds for large n. For a completely random arrangement, $M/4 = 1 - \varepsilon$, where ε is the voidage fraction, and $\tau = 1/\varepsilon$. This method is used to calculate the tortuosity within each of the 64 grid squares and these values are then averaged to yield an estimate of the value of the tortuosity of the whole pellet.

Diffusion Flux Method

This method simulates diffusion under a concentration gradient, typical of a Wicke–Kallenbach experiment. The voidage fraction and local tortuosity (using Eq. [2] above) are found in each of the grid squares as described earlier.
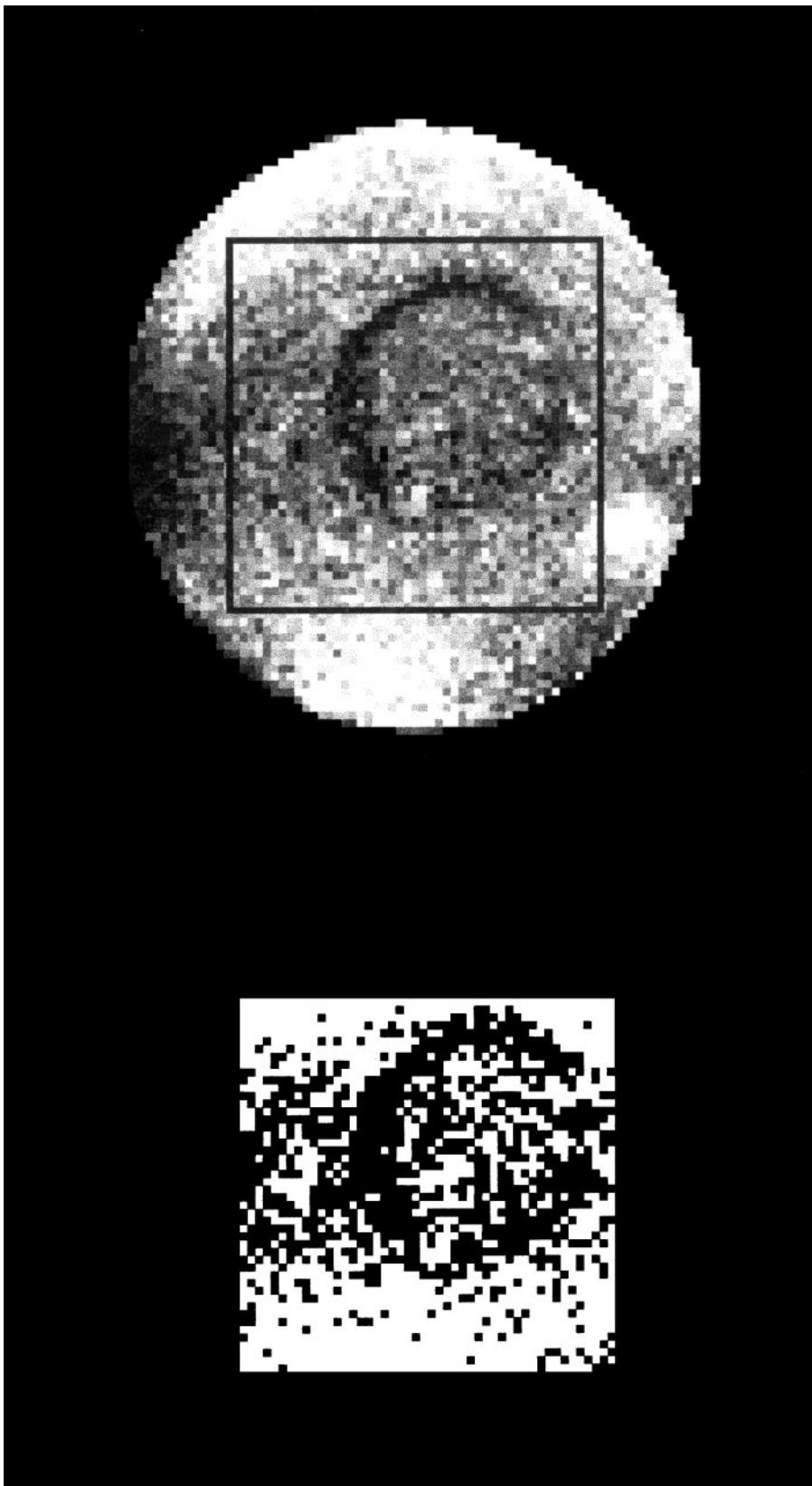
FIG. 1. Schematic representation of the construction of the simulation lattice. The spin density image (top) acquired for a pellet from batch E3 is shown (128 × 128 image, 1.0-mm slice, pixel = (40 μm)^2, echo time = 2.6 ms, repetition time = 1.5 s, number of scans = 40); higher intensity (white) pixels indicate higher spin density (voidage). The simulation lattice (bottom) is derived directly from the region identified with the image; matrix and void space are indicated by black and white pixels, respectively.

<div align="center">

TABLE 2

Comparison of Values of the Macroscopic Contribution to the Tortuosity as Determined by Experimental Measurement and Predicted Using the Strategy Described in the Text

</div>

Pellet	τ_{PGSE}	τ_{MRI}	τ_a	τ'_{WOA}	τ'_{DF}	τ'_a
E1 (3)	1.93 ± 0.22	Radial 2.05 ± 0.77 Axial 4.48 ± 0.61	1.04 ± 0.40	1.99 ± 0.11	2.07 ± 0.05	1.04 ± 0.06
E2 (3)	1.8 ± 0.2	Radial 2.3 ± 0.3 Axial 1.53 ± 0.19	1.28 ± 0.22	1.50 ± 0.01	1.80 ± 0.14	1.20 ± 0.1
E3 (3)	1.84 ± 0.12	Radial 2.4 ± 0.3	1.30 ± 0.18	1.51 ± 0.06	1.86 ± 0.13	1.23 ± 0.1
G1 (2)	2.04 ± 0.06	2.3 ± 0.1	1.15 ± 0.06	1.29 ± 0.05	1.52 ± 0.10	1.18 ± 0.08
G2 (2)	1.65 ± 0.35	1.8 ± 0.3	1.09 ± 0.3	1.37 ± 0.06	1.60 ± 0.05	1.17 ± 0.06

Note. The experimentally determined tortuosities from PGSE and MRI (τ_{PGSE}, τ_{MRI}) are used to determine the experimental prediction for the macroscopic contribution to the tortuosity (τ_a) (Eq. [12]). The predicted tortuosity from the whole object averaging (τ'_{WOA}) and diffusion flux (τ'_{DF}) simulations are used to predict the macroscopic contribution to the tortuosity (τ'_a) (Eq. [11]). All spin density images used in the generation of the simulation lattices were acquired in the radial direction. The number of pellets of each type studied is indicated in brackets; the errors are determined from the variations between measurements for the different pellets. The value of the tortuosity derived from PGSE NMR measurements for pellet E1 has been determined by considering a model for anisotropic diffusion (17) and by assuming that diffusion in the radial direction was much greater than diffusion along the axis of the pellet.

The two-dimensional steady-state diffusion equation,

$$\frac{\partial}{\partial X}\left[D(X,Y)\frac{\partial C}{\partial X}\right] + \frac{\partial}{\partial Y}\left[D(X,Y)\frac{\partial C}{\partial Y}\right] = 0;$$

$$D(X,Y) = \frac{\varepsilon(X,Y)D_A}{\tau(X,Y)}, \qquad [3]$$

where C is a dimensionless concentration, X and Y are dimensionless Cartesian coordinates, and D_A is the molecular diffusivity, is then solved for an applied gradient in the X direction by using a finite difference algorithm,

$$C_{i,j} = \frac{D_{i+1/2,j}\cdot C_{i+1,j} + D_{i-1/2,j}\cdot C_{i-1,j} + D_{i,j+1/2}\cdot C_{i,j+1} + D_{i,j-1/2}\cdot C_{i,j-1}}{D_{i+1/2,j} + D_{i-1/2,j} + D_{i,j+1/2} + D_{i,j-1/2}}, \qquad [4]$$

where $D_{i,j}$ is the diffusivity in the i, jth pixel. Once the values of concentration for all the grid squares have been found, the effective diffusivity, D_e, is calculated by averaging perpendicular to the direction of the applied gradient:

$$D_e = \int_0^L -D \cdot \frac{\partial C}{\partial X} \cdot dY, \qquad [5]$$

where L is the size of the simulation grid, and $\partial C/\partial X$ is obtained using a one-dimensional Taylor expansion,

$$\left(\frac{\partial C}{\partial X}\right)_{X=x} = \frac{C_{x+h,Y} - C_{x-h,Y}}{2h}, \qquad [6]$$

where h is the distance between the square centres (i.e., "length of step"). The average tortuosity factor is then calculated from

$$\langle \tau \rangle = \frac{\langle \varepsilon \rangle D_A}{D_e}. \qquad [7]$$

The results for the values of tortuosity predicted by both simulation techniques for pellets drawn from five different batches are given in Table 2.

NMR Measurements of Diffusion

Magnetic resonance techniques were used to provide two experimental determinations of diffusion within each of the porous catalyst pellets. The two techniques used were pulsed gradient spin echo (PGSE) NMR and magnetic resonance imaging. The theory upon which these methods are based, experimental details and analysis of results have been reported elsewhere (11, 15). The results of the experiments are given in Table 2. In the case of PGSE NMR techniques the self-diffusivity of water, D(pore), imbibed within the pore space of the catalyst pellet is measured, and the tortuosity of the material calculated as D(bulk water)/D(pore). In contrast, in the MRI approach, an initially water (^{1}H$_2$O)-saturated pellet is immersed in deuterated water (D$_2$O) and the transient exchange of the D$_2$O into the pellet measured. The ^{1}H$_2$O profiles are recorded as a function of time and then fitted to the appropriate diffusion equation, thereby providing an estimate of the diffusion coefficient of water under a concentration gradient, from which the tortuosity is calculated. By suitable preparation of the sample it is possible to measure this latter diffusion

coefficient in both the radial and axial directions through the pellet using the MRI method. In earlier work, we have used this technique to characterise diffusion anisotropy introduced into the pellet structure as a result of the manufacturing process (16).

Clearly there is no reason for the two measurements of PGSE NMR and MRI measurements of diffusion to be the same. However, if the PGSE NMR and MRI measurements of diffusion are numerically equivalent it would suggest that the heterogeneity in pore structure encountered over the lengthscales probed by the two types of magnetic resonance experiment are also the same. In the PGSE NMR experiment the relevant lengthscale is the root-mean-square displacement travelled by the water molecule during the timescale of the measurement, i.e. about 0.01 mm in these experiments. In contrast, the MRI experiment probes a lengthscale of the dimension of the pellet.

DISCUSSION

The results obtained suggest that this approach, in which the simulation lattice is derived directly from magnetic resonance images, is capable of predicting the trends in the experimentally determined values of tortuosity characterising the porous catalyst support pellets studied in this work. In rationalising the experimental and numerical studies additional insights regarding the detail of the pore structure of these materials are obtained.

In general, the total tortuosity, τ, of a porous solid can be considered to have independent contributions from tortuosity on various lengthscales. The total tortuosity can then be written as the product of these independent tortuosities since the effective diffusivity will decrease monotonically with scale—assuming that the material does not contain fractures or a distinct macropore/micropore structure. In this paper the total tortuosity will be written as

$$\tau = \tau_a \tau_e \tau_\mu, \qquad [8]$$

where τ_a is the macroscopic tortuosity describing the pore structure over lengthscales of the whole pellet (mm), τ_e is the mesoscopic contribution to the tortuosity which, say, describes tortuosity measured over lengthscales of a few pore diameters up to scales at which macroscopic heterogeneities become important, and τ_μ characterises tortuosity over lengthscales of up to a few pore diameters. The value of the mesoscopic contribution to the tortuosity can depend on the lengthscale probed by the PGSE NMR experiment but will take a single value for a given set of data acquisition parameters; in the current work the PGSE experiment probes scales of order 10 μm and the pore diameters are of order 0.01 μm. It is now possible to write expressions which identify the specific contributions to the values of tortuosity measured using the PGSE NMR and MRI techniques. The

PGSE experiment measures

$$\tau_{\mathrm{PGSE}} = \tau_e \tau_\mu \qquad [9]$$

while the MRI experiment measures

$$\tau_{\mathrm{MRI}} = \tau_a \tau_e \tau_\mu. \qquad [10]$$

In the case of the PGSE NMR experiment, diffusion within a porous material which is heterogeneous on a lengthscale greater than the root-mean-square displacement travelled by a water molecule during the timescale of the measurement will be characterised by a distribution of values of the diffusivity. The results (τ_{PGSE}) quoted in Table 2 are, therefore, obtained from the average value of the diffusivity obtained from a fitted distribution of diffusivity values (15). For completeness, a further set of experiments was performed in which a range of diffusion time values were used in the PGSE NMR experiments; the longer the diffusion time the larger the lengthscale probed during data acquisition. Hence we were able to assess the sensitivity of the mesoscopic contribution to the total tortuosity to the precise data acquisition parameters used. For example, for the cases of pellets G1 and G2 root-mean-square displacements in the range 9–34 and 10–39 μm, respectively, were probed. The values of diffusivity and, hence, tortuosity remained constant, to within experimental error for each sample.

Using an analogous approach to describe the values of tortuosity obtained from the diffusion simulations and denoting a quantity estimated by the models with a primed symbol, the whole object averaging method will estimate a tortuosity, $\tau'_{\mathrm{WOA}} = \tau'_e$, and the diffusion flux method will yield a tortuosity, $\tau'_{\mathrm{DF}} = \tau'_a \tau'_e$. Hence,

$$\tau'_a = \tau'_{\mathrm{DF}}/\tau'_{\mathrm{WOA}} \qquad [11]$$

and

$$\tau_a = \tau_{\mathrm{MRI}}/\tau_{\mathrm{PGSE}}. \qquad [12]$$

If the modelling methodology adopted in this work is valid and has predictive power then $\tau_a = \tau'_a$. Direct quantitative agreement between the results of the diffusion flux simulations and MRI evaluations of tortuosity will not be expected because the diffusion flux simulation does not reflect any microscopic contributions to the tortuosity which the MRI measurement will be sensitive too. The PGSE NMR and whole object averaging methods will not be expected to give quantitative agreement for the same reason.

Let us now consider the data in Table 2. Good agreement between experimental and predicted macroscopic tortuosities is observed for all pellets. The direct use of MRI images in the construction of simulation lattices used to predict macroscopic tortuosity therefore appears to offer significant potential. A further improvement to the modelling

strategy can be obtained by the use of fully three-dimensional MRI images in which the anisotropic properties of the macroscopic tortuosity are probed directly.

Further insights into the structure of the porous pellets studied can also be obtained from Table 2. An estimate of the microscopic tortuosity is obtained from the ratio $\tau_{\text{PGSE}}/\tau'_{\text{WOA}}$. Thus, the microscopic tortuosities for each pellet are estimated to be 1.0 for pellet E1, 1.2 for pellets E2, E3, and G2 and 1.6 for G1. This result suggests that pellet G1 has a significantly greater microscopic tortuosity than any of the other pellets studied here, which is consistent with the anomalously high pore surface area characterising this catalyst support. The striking difference in the anisotropy of pellets E1 and E2 can most readily be explained by consideration of their respective manufacturing processes. Pellet E1 has been formed by a tabletting process, whereas pellet E2 is produced using an extrusion process; the tabletting process might be expected to give a particularly high tortuosity in the axial direction (16).

CONCLUSIONS

Previous experimental work using magnetic resonance imaging techniques has shown that catalyst support pellets have a heterogeneous spatial distribution of voidage across them; distinct macroscopic regions exist with differing average voidage fraction. This paper has shown that the information extracted from the images is not restricted to a solely qualitative observation on the distribution of voidage heterogeneities in a pellet. It is demonstrated that detail is contained in the images which can be employed in representations of the real porous media imaged and consequently obviate the need for abstract or mathematical models of the structure of such porous materials. Whilst the gating procedure necessary to turn an image into a lattice suitable for the diffusion simulation methods chosen does lead to some loss in structural detail, the simulations give rise to good predictions of the macroscopic tortuosity for these porous materials. Comparison of this value with the experimental determinations of tortuosity from MRI and PGSE NMR experiments allows the relative contributions of the pore structure to the macroscopic and microscopic tortuosities of a given porous material to be assessed.

REFERENCES

1. Sharratt, P. N., and Mann, R., *Chem. Engng. Sci.* **42**, 1565 (1987).
2. Hollewand, M. P., and Gladden, L. F., *Chem. Engng. Sci.* **47**, 1761 (1992).
3. Hollewand, M. P., and Gladden, L. F., *Chem. Engng. Sci.* **47**, 2757 (1992).
4. Reyes, S. C., and Iglesia, E., *J. Catal.* **129**, 457 (1991).
5. Mace, O., and Wei, J., *Ind. Engng. Chem. Res.* **30**, 909 (1991).
6. Smith, B. J., and Wei, J., *J. Catal.* **132**, 21 (1991).
7. Smith, B. J., and Wei, J., *J. Catal.* **132**, 41 (1991).
8. Elias-Kohav, T., Sheintuch, M., and Avnir, D., *Chem. Engng. Sci.* **46**, 2787 (1991).
9. Coppens, M.-O., and Froment, G. F., *Chem. Engng. Sci.* **49**, 4897 (1994).
10. Hollewand, M. P., and Gladden, L. F., *J. Catal.* **144**, 254 (1993).
11. Hollewand, M. P., and Gladden, L. F., *Chem. Engng. Sci.* **50**, 327 (1995).
12. Gladden, L. F., Hollewand, M. P., and Alexander, P., *AIChE J.* **41**, 894 (1995).
13. Rigby, S. P., and Gladden, L. F., *Chem. Engng. Sci.* **51**, 2263 (1996).
14. Callaghan, P. T., "Principles of Nuclear Magnetic Resonance Microscopy," Oxford Univ. Press, Oxford, 1991.
15. Hollewand, M. P., and Gladden, L. F., *Chem. Engng. Sci.* **50**, 309 (1995).
16. Rigby, S. P., Cheah, K. Y., and Gladden, L. F., *Appl. Catal. A* **144**, 377 (1996).
17. Callaghan, P. T., Jolley, K. W., and Lelievre, J., *Biophys. J.* **28**, 133 (1979).